Global NEST Journal, **28** (8), 08658
Available online: 15/10/2026

Design and Chemical Fabrication of $Mo_xMn_{1-x}Fe_2O_4$/g-C_3N_4 Hybrid Nanocomposite for Photocatalytic Degradation of Direct Green 6 Dye: Environmental Cleaner Approach

Azqa Amjad[1], Shumaila Kiran[1]*, Muhammad Bilal Qadir[2], Shazia Abrar[1] and Muhammad Naveed Anjum[1]

[1]Department of Applied Chemistry, Government College University, Faisalabad, 38000, Pakistan
[2]Department of Textile Engineering, National Textile University, Faisalabad, Pakistan

*Correspondence e-mail: shumaila.asimch@gmail.com; shumailaasim@gcuf.edu.pk

Abstract

$Mo_xMn_{1-x}Fe_2O_4$/g-C_3N_4 nanocomposites (NCs) were fabricated using a hydrothermal approach by amalgamating mixed spinel ferrite ($Mo_xMn_{1-x}Fe_2O_4$) nanoparticles (NPs) with graphitic carbon nitride (g-C_3N_4) sheets to enhance photocatalytic performance under visible light. The synthesized materials were analyzed using XRD, SEM, EDX, FTIR, UV-visible spectroscopy, and zeta potential to show that the ferrite/g-C3N4 heterostructure was successfully formed. The $Mo_xMn_{1-x}Fe_2O_4$/g-C_3N_4 nanocomposites demonstrated superior degradation of Direct Green 6 (DG6) dye under visible light relative to the separate components, attributable to improved visible-light absorption and the effective separation of photogenerated electron-hole pairs. The Mo0.5Mn0.5Fe 2O4/g-C3N4 ratio was the most effective and was optimized using a central composite design (CCD). The maximum degradation rate of 97.35% was achieved with an ideal condition of the concentration of dye (0.01%), solution pH (10), H2O2 concentration (0.07 M), catalyst concentration (1 mg), and temperature (90 °C). The degradation process was a pseudo-first-order reaction, although the adsorption studies were found to be better fitted by the Langmuir model. The nanocomposite (NC) showed good reusability over five cycles, an effective ratio of TOC (83.6%), COD (79.1%), and good biocompatibility, showing that it could be used to treat wastewater in the long term. The Mo0.5Mn0.5Fe2O4/g-C3N4 heterostructured nanocomposite synthesized has significant role in the remediation of dye-contaminated wastewater since it is sustainable and recyclable.

Keywords: $Mo_xMn_{1-x}Fe_2O_4$ nanoparticles (NPs), $Mo_xMn_{1-x}Fe_2O_4$/g-C_3N_4 nanocomposites (NCs), Pollution, Direct Green 6 dye (DG6), Catalyst reusability.

OPEN ACCESS

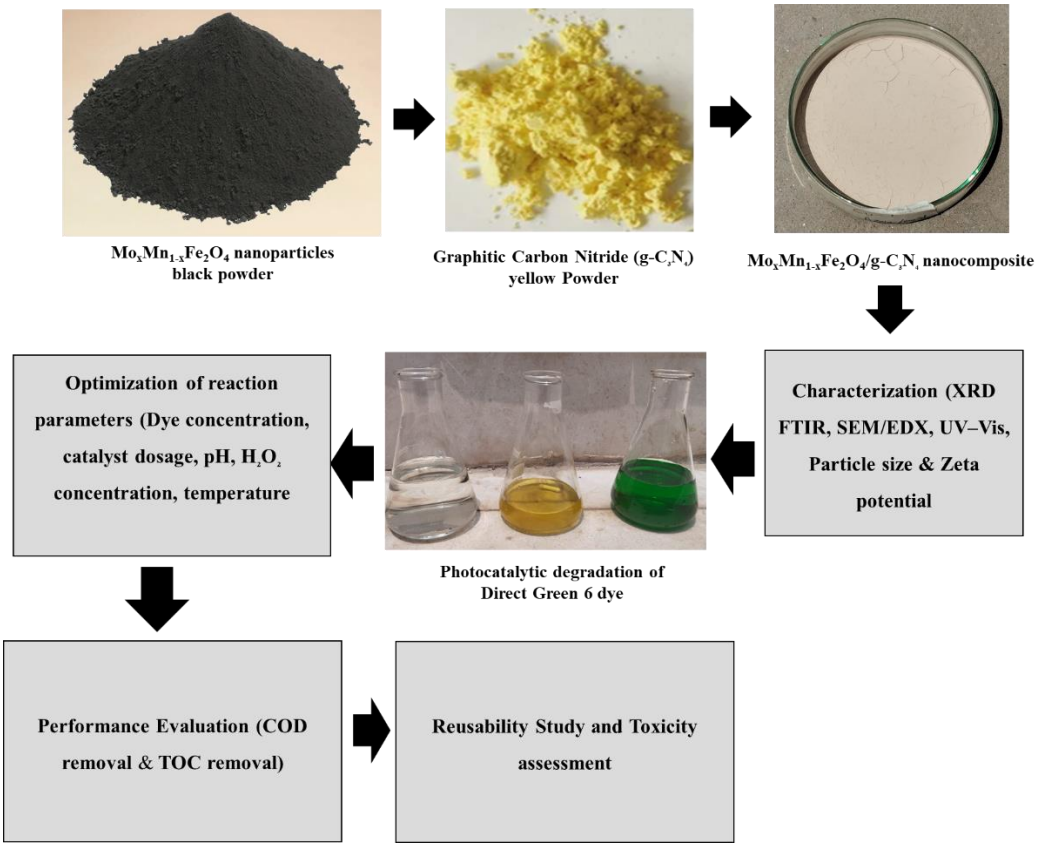
Received: 24/05/2026,

Accepted: 13/10/2026,

Available online: 15/10/2026

Copyright: © 2026 The Author(s). Published in Global NEST Journal. This article is licensed under the terms and conditions of the Creative Commons Attribution 4.0 International license (CC BY 4.0).

Graphical abstract



1. Introduction

The rapid industrialization, urbanization, and population growth are bringing environmental pollution to one of the most serious worldwide problems. In comparison with other forms of pollution, water pollution has been the most talked about due to the shortage of clean water and its continuous pollution by industries (Saxena *et al.* 2025). Various industries, such as textile, leather, paper, printing, food, and other dye industries, discharge significant volumes of colored wastewater into water bodies (Mukherjee *et al.* 2025). These effluents carry synthetic dyes, salts, organic additives, and other toxins, which have the potential to disrupt aquatic life and result in serious health impacts for humans (Iqbal, 2021).

Synthetic dyes are extensively used due to their high color brilliance, stability, and high binding ability with fabrics. These properties also make them hard to separate from wastewater. Numerous dyes are known to be resistant to light, heat, oxidation, and biodegradation, allowing them to last a long time in the environment (Kiran *et al.* 2025). At low concentration, dyes can decrease light penetration, interfere with photosynthesis, decrease dissolved oxygen, and affect the natural balance of aquatic ecosystems. Some dye molecules and degradation products can also be toxic, mutagenic, or carcinogenic (Naz *et al.* 2025).

Direct dyes are usually applied in textile fields such as cotton, silk, wool, viscose, leather, or other cotton fibers. One synthetic dye has strong water solubility and a complex molecular structure, making it difficult to remove from wastewater by normal treatment methods, and that is Direct Green 6 (De Oliveira *et al.* 2025). The release of Direct Green 6 dye into water bodies may cause environmental and health issues, so its extraction or degradation from polluted water is a crucial research issue (Gupta *et al.* 2020).

Different conventional techniques have been used for the removal of these dyes, such as adsorption, coagulation, flocculation, chemical oxidation, membrane filtering, biological treatment, ion exchange, and electrochemical processes (Kaur *et al.* 2025). These techniques can lower the concentration of the dye; there are some drawbacks, including high operating expenses, partial degradation, sludge production, secondary pollution, and low efficiency for highly stable molecules of dyes. For this reason, researchers have been directed towards advanced treatment technologies that can remove the color, along with breaking the dye molecules into less harmful products (Ahsan *et al.* 2025).

Photocatalysis is a more advanced form of oxidation that could be used to break down organic pollutants in wastewater. In this process, photon energy reacts with a semiconductor photocatalyst to make an electron-hole pair. This pair then interacts with oxygen and water to make reactive oxygen species (ROS) such as hydroxyl (**.**OH) and superoxide radicals (**.**O_2^-) (Rasool *et al.* 2025). These reactive species cause an attack on dye molecules to

change into less complex and less toxic compounds. Photocatalysis is a promising solution to wastewater treatment due to the ability to conduct the reactions under mild conditions (Solar or visible light) (Sinha *et al.* 2025).

MFe_2O_4 (M represents Fe, Ni, Co, Cu, and Mn) is one of the spinel ferrite nanomaterials that has gotten a lot of attention for use in photocatalytic applications because of its magnetic properties, chemical stability, tunable energy gap, and visible-light response (Singh, 2025). The degradation of organic dyes has been investigated using ferrite-based photocatalysts like $CoFe_2O_4$, $NiFe_2O_4$, $ZnFe_2O_4$, $MnFe_2O_4$, and mixed ferrite (Toqeer, 2026). They also possess magnetic properties, which allow for their separation from treated water when exposed to an external magnetic field. The photocatalytic activity of ferrite nanoparticles is restricted by the rapid recombination of the photo-generated electrons and holes, which leads to less degradation efficiency (Sharma *et al.* 2023).

The metal-free semiconductor graphitic carbon nitride (g-C_3N_4) has attracted considerable interest in environmental photocatalysis because of its suitable band gap, excellent capability to absorb visible light, thermal stability, low cost, and facile preparation process (Gupta *et al.* 2020; Iqbal *et al.* 2021; Ahsan *et al.* 2025). However, pristine g-C_3N_4 exhibits several limitations such as poor specific surface area, low photocatalytic efficiency and fast coupling photogenerated charge carriers, low photocatalytic efficiency, and low specific surface area. To address these drawbacks, g-C_3N_4 has been integrated with metal oxides, metal ferrites, and other semiconductor materials to form heterojunction photocatalysts. These composite systems can enhance the interfacial transfer of charges, increase visible-light incorporation, and reduce charge reintegration. Therefore, this improves the rate of photocatalytic degradation performance (Shahverdizadeh *et al.* 2025).

Recent studies have shown that incorporation of g-C_3N_4 with ferrite-based nanomaterials is an efficient approach for improving photoactivity by increasing charge separation and accelerating interfacial electron migration (Arunprasad *et al.* 2026). The degradation of several organic dyes using Ferrites/g-C_3N_4 heterojunctions such as $CoFe_2O_4$/g-C_3N_4, $MnFe_2O_4$/g-C_3N_4 materials have shown that visible light can break down these dyes more efficiently with their respective components (Akechatree *et al.* 2025; El-Sayyad *et al.* 2020). This improved activity is mostly due to the creation of heterojunction interfaces, better light absorption, and efficient use of charge carriers that are created by light. However, molybdenum-modified manganese ferrites mixed with g-C_3N_4 have not been studied very much especially when it comes to photocatalytic degradation of Direct Green 6 dye (DG6). Therefore, $Mo_xMn_{1-x}Fe_2O_4$/g-C_3N_4 nanocomposites require further research to determine how the addition of molybdenum affects structural characteristics, charge transfer behavior and photocatalytic efficiency. Molybdenum-containing ferrite materials have been of great interest as molybdenum can affect the structural, optical, and surface properties of photocatalysts (Bakht *et al.* 2025; Afzal *et al.* 2021)) When molybdenum added to manganese ferrite, it can change the band structure, generate active sites and make it easier for of photogenerated charge carriers to move freely. When these ferrite nanoparticles are mixed with g-C_3N_4, they can better absorb visible-light and reduce the electron-hole recombination from the g-C_3N_4. This material can make it easier for the degradation of Direct Green 6 dye in wastewater.

Unlike previously reported ferrites/g-C_3N_4 photocatalysts, which mainly focus on $CoFe_2O_4$, $ZnFe_2O_4$, and $MnFe_2O_4$ systems (Ma & Liu, 2021). The present study describes molybdenum-incorporated manganese ferrite ($Mo_XMn_{1-x}Fe_2O_4$) with g-C_3N_4. Molybdenum incorporation can modify the electronic structure by creating active sites and making it easier for visible-light to pass through and for charges to separate. Furthermore, the systematic analysis of various Mo concentration levels (x=0.1 to 0.5) and optimization of Direct Green 6 degradation with CCD make this work different from previously reported ferrites/g-C_3N_4. However, limited studies have examined ($Mo_XMn_{1-x}Fe_2O_4$) with g-C_3N_4 nanocomposites, and how the introduction of molybdenum affects the structural, optical, photocatalytic characteristics is not well understood. Therefore, further investigation is required to determine the relationship between material composition, physicochemical properties, and photocatalytic degradation efficiency (Praus *et al.* 2022).

In the present study, we systematically synthesized and evaluated $Mo_xMn_{1-x}Fe_2O_4$/g-C_3N nanocomposites with varying molybdenum ratios (x=0.1, 0.2, 0.3, 0.4 and 0.5) for the visible-light-driven degradation of Direct Green 6. Comprehensive characterization (XRD, FTIR, SEM, EDX, Zeta Potential, and UV-vis spectroscopy) was carried out to study their structural, functional, and optical features. This research offers a valuable method to design ferrite/g-C_3N_4 photocatalysts for the decontamination of dye-contaminated wastewater (Sun *et al.*, 2022). This research aims to create an effective, stable, and eco-friendly photocatalyst for the treatment of wastewaters contaminated with dyes (Michalska *et al.*, 2024; Lu *et al.* 2022).

2. Experimental

2.1. *Materials*

The reagents and chemicals used in the current study were of analytical grade. The Direct Green 6 dye (DG6) was commercially purchased from Faisalabad, Pakistan and utilized without any additional purification to conduct photocatalytic experiments.

2.2. *Materials Synthesis Methods*

2.2.1. Synthesis of Graphitic Carbon Nitride (g-C_3N_4)

g-C_3N_4 was prepared by the thermal polymerization process using melamine as the precursor (Joseph *et al.* 2026). 10g of melamine (Sigma-Aldrich, analytical grade) was precisely measured and placed into an alumina crucible. The sealed crucible was placed inside a tube

furnace, under a constant flow of nitrogen (N_2). This nitrogen gas created a non-reactive (inert) atmosphere during the synthesis process. To ensure the melamine was polymerizing, the furnace temperature was increased to 550 °C at a heating rate of 5 °C/min and maintained at this temperature for 3-4 hours. After completion of the reaction, the furnace was allowed to return to ambient temperature. The obtained yellow g-C_3N_4 powder was collected and stored for further composite synthesis (Akhtar *et al.* 2024; Hassanzadeh *et al.* 2023). During the heating process, gradual decomposition of melamine occurred with the release of gaseous products, resulting in the appearance of white fumes inside the furnace tube and deposition of condensed material on the inner surface. The white melamine precursor gradually transformed into a yellow powder, confirming the formation of graphitic carbon nitride. After cooling to room temperature, the yellow g-C_3N_4 powder was collected. The g-C_3N_4 precursor (melamine/urea) is a low-cost, nitrogen-rich, and non-hazardous material, and its thermal polycondensation did not require any chemical activating or reducing agents. No toxic or hazardous by-products were generated during the fabrication process.

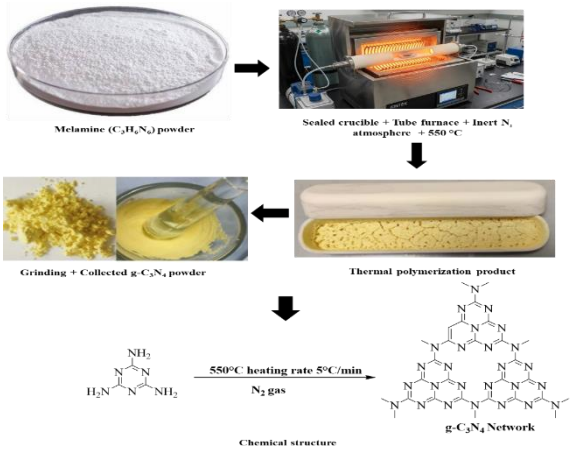


Figure 1. Synthesis of g-C_3N_4

2.2.2. Synthesis of $Mo_xMn_{1-x}Fe_2O_4$ nanoparticles

Molybdenum manganese ferrite nanoparticles ($Mo_xMn_{1-x}Fe_2O_4$) were synthesized through a hydrothermal method with molybdenum (Mo) content varying from x = 0.1 to 0.5. Iron (III) nitrate nonahydrate ($Fe(NO_3)_3$. $9H_2O$), Manganese (II) nitrate tetrahydrate ($Mn(NO_3)_2$. $4H_2O$), and ammonium heptamolybdate tetrahydrate ($(NH_4)_6Mo_7O_{24}$. $4H_2O$) were used as metal precursors salts. A 0.1% solution of polyvinyl pyrrolidone (PVP) was used as a capping agent. In three separate beakers, 50 mL of deionized water was added to dissolve each metal precursor. All precursors' solutions were stirrer until complete dissolution. The pH of molybdenum precursor solution was adjusted to 6.5. PVP solution was mixed with iron (Fe) solution. Then Mo and Mn solutions were added dropwise to the Fe solution, ensuring thorough mixing. Ammonia (NH_3) solution was used to rise the pH of iron (Fe) mixture up to 9 to ensure that ferrite could form and molybdenum could stay in the solution. The obtained solution was poured into an autoclave. Then the autoclave was tightly sealed and heated at 180 °C for the duration of 24 hours. After the hydrothermal reaction, the mixture was cooled, rinsed thrice with deionized water, and once with ethanol to remove contamination. The cleaned product was dried at 80 °C for 24 h and then calcined at 500 °C for 5 h in a muffle furnace. The final nanoparticles were ground to a fine powder and stored for further characterization (Khaliq *et al.* 2026). This hydrothermal method was carried out in an aqueous system, avoiding the need for toxic organic solvents.

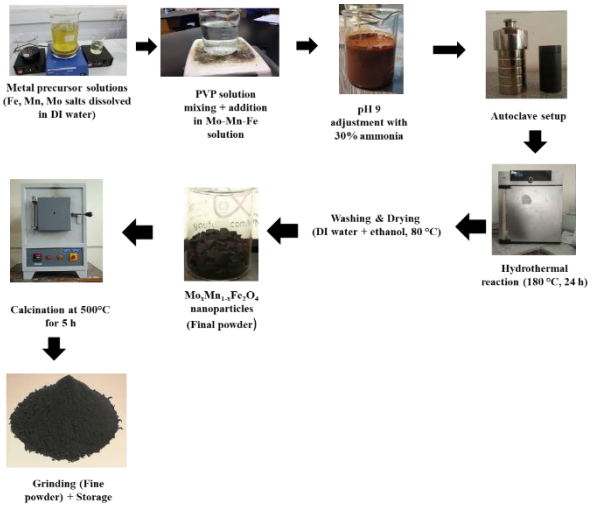


Figure 2. Synthesis of $Mo_xMn_{1-x}Fe_2O_4$ nanoparticles (NPs)

2.2.3. Synthesis of $Mo_xMn_{1-x}Fe_2O_4$/ g-C_3N_4 nanocomposite

The **$Mo_xMn_{1-x}Fe_2O_4$/g-C_3N_4 nanocomposite** was synthesized by mixing **30 wt% $Mo_xMn_{1-x}Fe_2O_4$ nanoparticles** with **70 wt% g-C_3N_4. 15 mL of ethanol** was used to dissolve both materials separately in two beakers. The nanoparticle solution was mixed with g-C_3N_4 solution, and then the combined mixture was sonicated for **30 minutes**. The mixture was transferred into the petri dish for drying (overnight). Once the composite was fully dried, it was stored in a sample vial for further characterization (Khaliq *et al.* 2026).

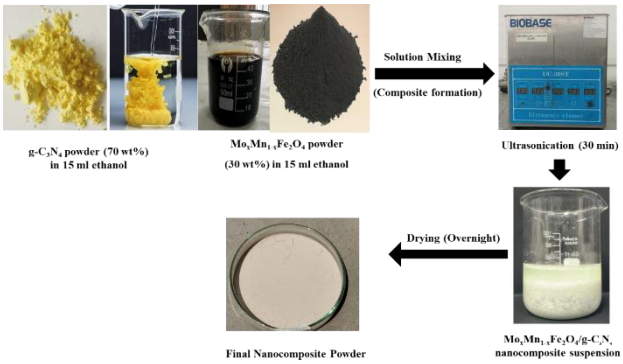


Figure 3. Synthesis of **$Mo_xMn_{1-x}Fe_2O_4$/g-C_3N_4** nanocomposites (NCs)

3. Preliminary Dye Degradation and Selection of Optimal Nanocomposite

Preliminary dye degradation trials were conducted for five different $Mo_xMn_{1-x}Fe_2O_4$/g-C_3N_4 (x=0.1-0.5) using Direct Green 6 dye. Among the various compositions, the $MO_{0.5}Mn_{0.5}Fe_2O_4$/g-C_3N_4 nanocomposite exhibited the

highest degradation activity, and thus, it was selected for further analysis.

4. Characterization techniques

The selected $MO_{0.5}Mn_{0.5}Fe_2O_4$/g-C_3N_4, $MO_{0.5}Mn_{0.5}Fe_2O_4$, g-C_3N_4 were characterized to evaluate its structural, optical, and surface features using various techniques. **FTIR** was employed for functional group identification, while **UV-Visible Spectroscopy** analyzed its optical absorption properties. The **morphology and particle size distribution** were examined through **SEM**, and **EDX** provided insights into its elemental composition. The **Zeta Potential** measurements determined the particle size distribution, surface charge density, and **XRD** was used to evaluate the crystal and phase structure of the materials (Lu *et al.* 2022).

5. Application of $Mo_xMn_{1-x}Fe_2O_4$/g-C_3N_4 for the remediation of Direct Green 6 dye

5.1. *Scanning of λ_{max}*

Absorbance readings were taken to scan λ_{max}. For this purpose, solutions with varying dilutions (10-100 ppm) were prepared, and the absorbance of these solutions was determined by measuring them in the UV-Visible spectrophotometer (Kiran *et al.* 2025).

5.2. *Experimental procedure*

To the flask, 0.01% of the direct dye solution was added, to the flask and 3 mg of $Mo_xMn_{1-x}Fe_2O_4$/g-C_3N_4 nanocomposite was then placed in the flask. Then 1 molar NaOH and 0.1 molar H_2SO_4 were used to change the pH of the solution from 4 to 10. A flask that was containing the dye solution and nanocomposite (measured amount) was placed on a stirrer plate for 70 min. To find the optimum methodology of the same, the absorbance after every 10 minutes was measured for various concentrations of dye (0.01-0.07%), $Mo_xMn_{1-x}Fe_2O_4$/g-C_3N_4 nanocomposite (1-7 mg), H_2O_2 (0.01-0.07 M), pH (4-10), and temperature (30-90 ℃). Other parameters were kept fixed, and only one parameter was changed in each trial (Kiran *et al.* 2025).

The developed photocatalytic system represents an environmentally cleaner approach because it utilizes visible light as an energy source, employs a recyclable magnetic catalyst, and promotes degradation of organic pollutants without generating excessive secondary waste (Pattanayak et al., 2024).

5.3. *Chemical analysis*

A UV-visible spectrophotometer was used to find the absorbance at 624 nm. The absorbance of the solution was quantified, which gave the % of decolorization. The % of decolorization was calculated by using the formula below (Naz *et al.* 2025).

Decolorization (%) + (I-F)/I×100

5.4. *Mineralization study*

The total organic carbon (TOC) and Chemical oxygen demand (COD) is used to find out how much dye was in the treated and untreated solutions, by using the protocols mentioned in the paper by researchers (Naz *et al.* 2025).

5.5. *Reusability of catalyst*

The synthesized NCs were reused to test its stability, performance, and functionality as a catalyst following the breakdown of the Direct Green 6 dye. Catalyst was filtered and rinsed three time with distilled water to eliminate synthetic dyes. After that thoroughly washed with ethanol to remove inorganic and organic impurities. The degradation of the target dye was then repeated with the catalyst. It was done four times until a significant reduction of dye degradation was seen (Kiran *et al.* 2025). The catalyst demonstrated good reusability/stability over multiple cycles with minimal loss in photocatalytic efficiency, reducing catalyst waste and supporting sustainable, repeated use.

5.6. *Dye degradation and statistical analysis*

The breakdown of the dye was evaluated through various stages, such as the breakdown of the old bonds and the formation of new compounds. The analysis was done statistically, and the results were calculated using standard error (Kiran *et al.* 2023).

Table 1. Different parameters of dye degradation

Sr No	A (Conc. of dye %)	B (Catalyst dose mg)	C (pH)	D (H2O2 M)	E (Temperature °C)
1	0.01	1	4	0.01	30
2	0.02	2	5	0.02	40
3	0.03	3	6	0.03	50
4	0.04	4	7	0.04	60
5	0.05	5	8	0.05	70
6	0.06	6	9	0.06	80
7	0.07	7	10	0.07	90

6. Results and Discussion

6.1. *Characterizations of $Mo_{0.5}Mn_{0.5}Fe_2O_4$ nanoparticles and $Mo_{0.5}Mn_{0.5}Fe_2O_4$/g-C_3N_4 nanocomposites*

6.1.1. UV-Visible spectroscopy

The absorption range of pristine g-C_3N_4, $Mo_{0.5}Mn_{0.5}Fe_2O_4$ nanoparticles, and $Mo_{0.5}Mn_{0.5}Fe_2O_4$/g-C_3N_4 are illustrated in figure no 4. The g-C_3N_4 showed a high absorption peak in the UV spectrum, which is explained by the π→π* electronic transition of the conjugated C-N heterocyclic structure. Moreover, the absorption peak of g-C_3N_4 shifted to the visible area, indicating the semiconductor nature of this material and its capacity to take advantage of visible-light irradiation. The $Mo_{0.5}Mn_{0.5}Fe_2O_4$ nanoparticles were able to absorb a lot of visible-light. This is because they

have a spinel ferrite structure and a small band-gap. When $Mo_{0.5}Mn_{0.5}Fe_2O_4$ was coupled with g-C_3N_4, the nanocomposite exhibited both optical properties of the two materials, but with increased absorption intensity in the visible region. This higher absorption of visible-light shows that the $Mo_{0.5}Mn_{0.5}Fe_2O_4$ nanoparticles and g-C_3N_4 sheets interact strongly with each other. This may speed up the movement of charges and stop the photogenerated electron-hole pairs from recombining. This higher absorption of visible-light shows that the consequently, the improved optical response of the $Mo_{0.5}Mn_{0.5}$ Fe_2O_4/g-C_3N_4 heterostructure also leads to its enhanced photocatalytic degradation efficiency when irradiated by visible-light. The same improved optical characteristics have been described in ferrite-based g-C_3N_4 heterojunction photocatalysts (Nguyen *et al.* 2025; Cao *et al.* 2017; Bondareko *et al.* 2020; C Devi and Soibam, 2017).

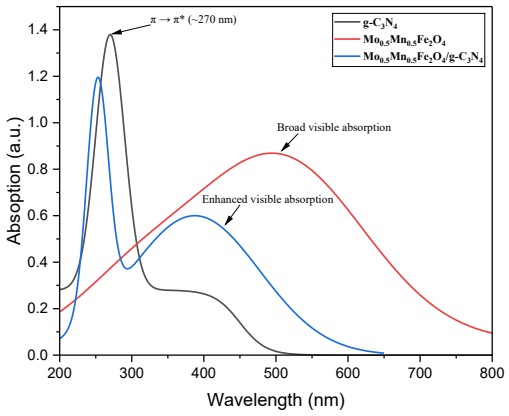


Figure 4. Comparison UV-visible graph of (a) pristine g-C_3N_4, (b) $Mo_{0.5}Mn_{0.5}Fe_2O_4$ nanoparticles, (c) $Mo_{0.5}Mn_{0.5}Fe_2O_4$/g-C_3N_4 nanocomposites.

6.1.2. X-ray diffraction (XRD)

The crystal lattice and structural state of synthesized $Mo_{0.5}Mn_{0.5}Fe_2O_4$ nanoparticles and $Mo_{0.5}Mn_{0.5}Fe_2O_4$/g-C_3N_4 nanocomposites were investigated using XRD. The corresponding XRD patterns of XRD are illustrated in Figure 5. The x-ray pattern of $Mo_{0.5}Mn_{0.5}Fe_2O_4$ displays diffraction peaks associated with the (220), (311), (400), (422), (511), and (440) planes of the cubic spinel ferrite structure at approximately 20 values of 30.2 °, 35.6 °, 43.2 °, 53.5, 57.2 °, and 62.8 °, with no new phase appearing, confirming that the ferrite is anchored on the g-C_3N_4 matrix rather than reacting to form a separate compound. These typical reflections are evidence that the spinel ferrite phase has been formed. The sharp (311) diffraction peak shows the high crystallinity of the ferrite nanoparticles synthesized, whereas the broadening of the diffraction peaks indicates the nanoscale crystalline nature of the synthesized material. Moreover, no further diffraction peaks were found, which means that secondary crystalline phases could not be produced in the course of the synthesis.

The XRD peaks of $Mo_{0.5}Mn_{0.5}Fe_2O_4$/g-C_3N4 NC show the diffraction characteristics of both spinel ferrite and the graphitic carbon nitride (GCN). The large diffraction band seen in the lower 20 (θ) range (1530) is due to the (002) diffraction plane of g-C_3N_4, which is formed by the interlayered stacking of the conjugated aromatic structures. A measurable shift/broadening of the ferrite peaks relative to the pristine ferrite reflects interfacial lattice strain from close ferrite–g-C_3N_4 contact, an approach used to confirm compositionally analogous g-C_3N_4/$Zn_xMn_{1-x}Fe_2O_4$ heterostructures (Manohar *et al.* 2026). In the meantime, the typical diffraction peaks of $Mo_{0.5}Mn_{0.5}Fe_2O_4$ remain visible in the composite, which indicates that the crystal structure of the ferrite phase is not lost throughout the integration with $g\text{-}C_3N_4$. The comparative graph (**Figure 2**) of XRD confirms the absence of new diffraction peaks. The absence of peaks shows that the phase of the prepared heterostructure is stable. The successful formation of the Mo0.5Mn0.5Fe_2O_4/g-C_3N_4 heterostructure was confirmed by the combined evidence obtained from XRD, FTIR, SEM and EDX analyses (Harikrishnan & Rajaram, 2024).

When g-C_3N_4 was added, the peak intensity decreased, and the diffraction peaks got bigger. This is because ferrite nanoparticles and the carbon nitride structure interacted with each other. This interaction suggests effective surface bonding between $Mo_{0.5}Mn_{0.5}Fe_2O_4$ and g-C_3N_4, which can facilitate electron transfer and reduce the recombination of photogenerated electron-hole pairs during light-induced catalytic reactions. Ferrite/g-C_3N_4-based heterojunction photocatalysts have been reported to have similar structural features, with the development of a close interface between ferrite and g-C_3N_4 helping to enhance photocatalytic activity. These results are supported by literature (Bharathi *et al.* 2024; Mazaheri *et al.* 2025).

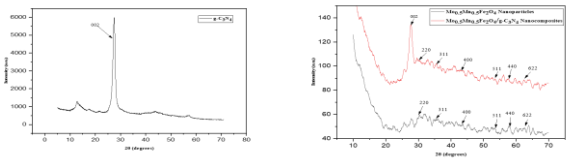


Figure 5. XRD images of (a) pristine g-C_3N_4 (b) $Mo_{0.5}Mn_{0.5}Fe_2O_4$ nanoparticles, $Mo_{0.5}Mn_{0.5}Fe_2O_4$/g-C_3N_4 nanocomposites,

6.1.3. Scanning Electron Microscope (SEM)

The surface morphology and structure of pristine g-C_3N_4, $Mo_{0.5}Mn_{0.5}Fe_2O_4$ nanoparticles and $Mo_{0.5}Mn_{0.5}Fe_2O_4$/g-C_3N_4 nanocomposite were analyzed using SEM, with the corresponding picture shown in Figure 6. This shows the ferrite nanoparticles uniformly decorating the g-C3N4 sheets rather than existing as a segregated phase. The results of the scanning electron microscopy show that the nanoparticles of $Mo_{0.5}Mn_{0.5}Fe_2O_4$ are effectively deposited onto the g-C_3N_4 surface. The ferrite NPs at a higher magnification are visible as scattered on the surface of the g-C_3N_4 sheets, which suggests that the two components have been in contact with each other. The even distribution of ferrite nanoparticles on the carbon nitride framework offers additional exposed interfacial sites that have the ability to interact with the photocatalyst surface and the dye molecules in the process of photocatalytic degradation.

In lower magnifications, slight aggregation of nanoparticles is visible and is usually observed with ferrite-based nanomaterials because of the magnetic interactions

between nanoparticles. However, the general structure of the composite is homogeneous, which is an indication of the effective inclusion of $Mo_{0.5}Mn_{0.5}Fe_2O_4$ into the g-C_3N_4 structure. The close association of ferrite hybrid materials and g-C_3N_4 sheets is favorable to interfacial charge migration and enhanced photocatalytic activity. These morphological features have been observed in cases of ferrite/g-C_3N_4 heterojunction photocatalysts, in which the homogeneous distribution of ferrite nanoparticles on g-C_3N_4 improves the contact between the two semiconductor materials and leads to a higher photocatalytic activity. These findings are compared with the literature (Salem *et al.* 2026; Mazaheri *et al.* 2025).

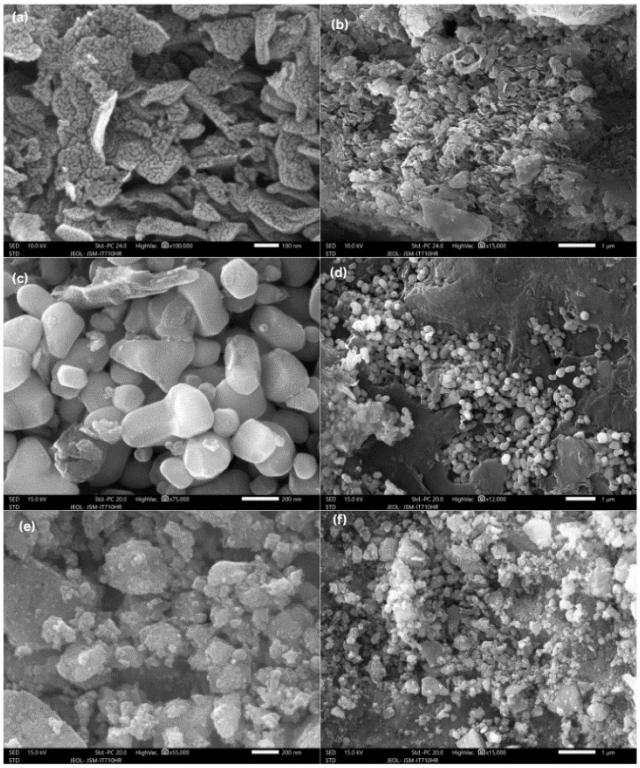


Figure 6. SEM analysis of (a) and (b) g-C_3N_4, (c) and (d) $Mo_{0.5}Mn_{0.5}Fe_2O_4$ nanoparticles, (e) and (f) $Mo_{0.5}Mn_{0.5}Fe_2O_4$/g-C_3N_4 nanocomposites.

6.1.4. EDX

The elemental composition of g-C_3N_4, $Mo_{0.5}Mn_{0.5}Fe_2O_4$ nanoparticles, and $Mo_{0.5}Mn_{0.5}Fe_2O_4$/g-C_3N_4 nanocomposites were studied by EDX, as shown in **Figure 7**. The spectrum of g-C_3N_4 (**Figure 7 (a)**) had characteristic signals of carbon (C) and nitrogen (N), illustrating the formation of carbon nitrate framework. The other elemental signals are absent, which shows the purity of the synthesized g-C_3N_4 material. The EDX spectrum of $Mo_{0.5}Mn_{0.5}Fe_2O_4$ nanoparticles (**Figure 7b**) had typical peaks of molybdenum (Mo), manganese (Mn), iron (Fe) and oxygen (O). These elements prove the existence of the mixed metal oxide ferrite composition. The presence of an oxygen signal along with Fe, Mn and Mo peaks suggests that the synthesized ferrite phase was an oxide whereas there were no other impurity-specific peaks. For $Mo_{0.5}Mn_{0.5}Fe_2O_4$/g-C_3N_4 nanohybrid material (**Figure 7 (c)**) the constituents of N, C, Mo, Mn, Fe and O were observed in the EDX spectrum. The presence of C and N of g-C_3N_4 and Mo, Mn, Fe, and O of the ferrite component proves the successful combination of the two phases in the composite. The elemental composition of the EDX analysis is consistent with the desired composition of the prepared heterostructure. The EDX findings corroborate the XRD and SEM results by showing the existence of ferrite and g-C_3N_4 elements in the nanocomposite. The existence of the two phases in the composite indicates effective interfacial contact of the $Mo_{0.5}Mn_{0.5}Fe_2O_4$ nanoparticles and g-C_3N_4 sheets, which is desirable in photocatalytic applications. EDX mapping (**Figure 7**) shows homogeneous spatial overlap of Mo, Mn, Fe, O with C and N, confirming intimate nanoscale contact between the two phases rather than macroscopic phase separation, as similarly demonstrated for the analogous g-C_3N_4/$Zn_xMn_{1-x}Fe_2O_4$ system (Manohar *et al*. 2026). Other elemental attributes have been indicated: ferrite/g-C_3N_4 based photocatalytic systems have been reported to have similar elemental characteristics, with the incorporation of ferrite nanoparticles with carbon nitride offering an effective platform on which photocatalytic performance can be enhanced. This discussion is supported by Horta *et al.* (2025).

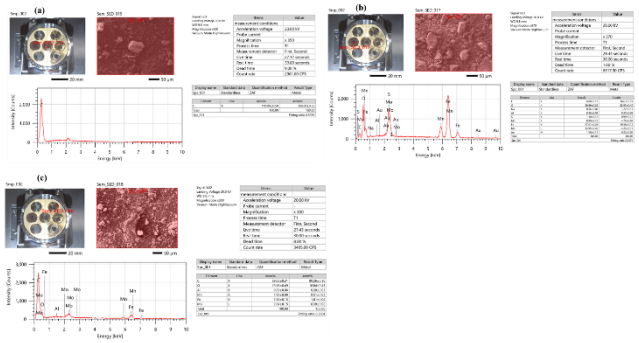


Figure 7. EDX analysis of (a) g-C_3N_4, (b) $Mo_{0.5}Mn_{0.5}Fe_2O_4$ nanoparticles, (c) $Mo_{0.5}Mn_{0.5}Fe_2O_4$/g-C_3N_4 nanocomposites.

6.1.5. FTIR

The spectra of pristine g-C_3N_4, $Mo_{0.5}Mn_{0.5}Fe_2O_4$ nanoparticles, and $Mo_{0.5}Mn_{0.5}Fe_2O_4$/ g-C_3N_4 nanocomposite are presented in **Figure 8**. The spectrum peaks of g-C_3N_4 show characteristic absorption bands associated with the carbon nitride framework. O-H/N-H stretching vibrations that could be due to surface hydroxyl groups, adsorbed water molecules, or terminal amino groups explain the wide band in the spectrum between 3200 cm^{-1} and 3400 cm^{-1}. The bands observed in the 1200-1650 cm^{-1} range are due to the stretching vibrations of C-N and C=N bonds in the conjugated heterocyclic ring system of g-C_3N_4. Moreover, the distinctive band at around 810 cm^{-1} is attributed to the vibration of the triazine units, thus establishing the establishment of the graphitic carbon nitrate structure.

The FTIR spectrum of $Mo_{0.5}Mn_{0.5}Fe_2O_4$ nanoparticles has characteristic absorption bands in the low wavenumber region. The bands that are seen around 400-600 cm^{-1} are attributed to metal-oxygen (M-O) vibrations of the spinel ferrite structure at tetrahedral and octahedral positions. The presence of these typical vibrations indicates the occurrence of the ferrite phase. The FTIR spectrum of the $Mo_{0.5}Mn_{0.5}Fe_2O_4$/g-C_3N_4 nanocomposite reveals the

characteristic features of both ferrite and g-C_3N_4. The preservation of C N / C =N and C=N stretching vibrations (1200-1650 cm^{-1}) and triazine ring vibration (~810 cm^{-1}) and metal-oxygen vibrations (400-600 cm^{-1}) is evidence of the successful combination of both components in the composite structure. The composite spectrum shows the g-C_3N_4 heptazine vibrations (~1200–1650 cm^{-1}) and C–N breathing mode (~810 cm^{-1}) together with the ferrite's M–O stretching band (~400–600 cm^{-1}); shifts in these bands relative to the pure components indicate M–O···N/C interfacial interaction rather than physical blending, consistent with characterization protocols used for $NiFe_2O_4$@P-doped g-C_3N_4 (Mishra *et al*. 2019). The minimal differences in peak intensity and position following the formation of the composite can be explained by the interaction between $Mo_{0.5}Mn_{0.5}Fe_2O_4$ nanoparticles with the g-C_3N_4 framework. The presence of both organic and inorganic vibrational characteristics proves the effective production of the ferrite/ g-C_3N_4 heterostructure. Ferrite-based g-C_3N_4 photocatalytic composites have been reported to have similar FTIR properties (Hassandzadeh *et al.* 2023; Bakht *et al.* 2025).

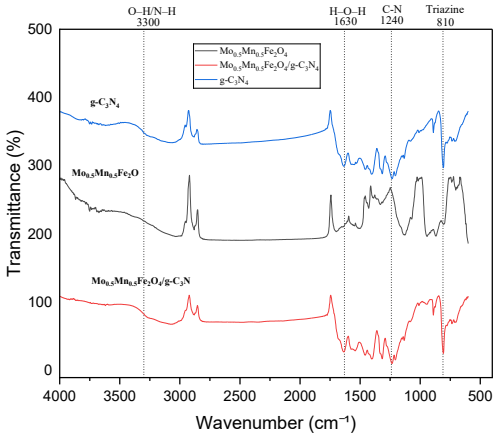


Figure 8. Comparison of FTIR spectrum of pristine g-C_3N_4, $Mo_{0.5}Mn_{0.5}Fe_2O_4$ nanoparticles, and their $Mo_{0.5}Mn_{0.5}Fe_2O_4$/g-C_3N_4 nanocomposites.

6.1.6. Estimation of Zeta potential and Particle size

The particle size distribution of pristine g-C_3N_4, $Mo_{0.5}Mn_{0.5}Fe_2O_4$ nanoparticles, and $Mo_{0.5}Mn_{0.5}Fe_2O_4$/g-C_3N_4 nanocomposite was investigated using dynamic light scattering (DLS), as shown in **Figure 9**. DLS analysis gives the hydrodynamic diameter of dispersed particles that tends to be higher than the actual particle size because of particle aggregation, surface hydration, as well as, contact with the dispersion medium. The g-C_3N_4 sample had a rather wide size distribution of the particles with a Z-average hydrodynamic diameter of about 870.4 nm). This is due to the layered structure of g-C_3N_4 where the nanosheets are likely to stack to each other during dispersion leading to higher hydrodynamic dimensions.

The particle size was found to be around 715.1 nm in Z-average with a narrow distribution of the $Mo_{0.5}Mn_{0.5}Fe_2O_4$ NPs. The presence of a larger hydrodynamic size than the nanoscale crystallite size can be attributed to aggregation of ferrite nanoparticles in the suspension because of magnetic dipole interactions and a high-energy substrate. After the formation of the $Mo_{0.5}Mn_{0.5}Fe_2O_4$/g-C_3N_4 NCs, the hydrodynamic size decreased to approximately 432.8 nm. This modification suggests the fact that the interactions between ferrite nanoparticles and g-C_3N_4 sheets affect the aggregation process and dispersion properties of the composite. These interactions of ferrite nanoparticles with the g-C_3N_4 structure might inhibit the over-clustering of the particles and ensure a more stable dispersed structure than the separate components. The variation between the DLS values and the sizes of particles measured by the microscopic methods is anticipated since DLS is used to measure the hydrodynamic diameter of the particles suspended in the suspension, not the original size of the particles. Overall, the results of the DLS justify the effective alteration of the dispersion behavior of the composite upon formation and justify the formation of an integrated $Mo_{0.5}Mn_{0.5}Fe_2O_4$/g-C_3N_4 heterostructure with better suspension stability, which can facilitate the contacting of catalyst particles and dye molecules during photocatalytic degradation (Wang *et al.* 2024; Akechatree *et al.* 2025).

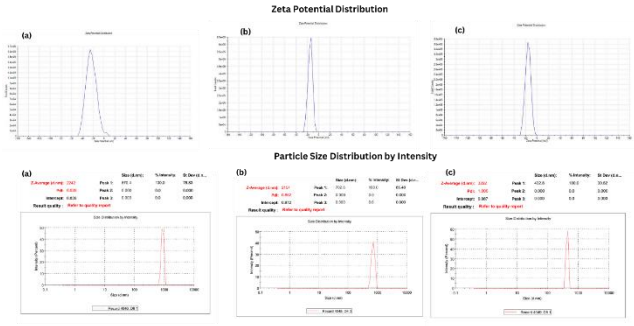


Figure 9. Zeta potential and Particle size distribution (intensity-based) of (a) g-C_3N_4, (b) $Mo_{0.5}Mn_{0.5}Fe_2O_4$ nanoparticles, (c) $Mo_{0.5}Mn_{0.5}Fe_2O_4$/g-C_3N_4 nanocomposites.

6.2. *Scanning of* λ_{max}

The wavelength of maximum absorption was selected by preparing a series of dye solutions of varying concentrations. The absorbance of all dye solutions was determined at various wavelengths. The λ_{max} was found to be 624 nm (**Figure 10**).

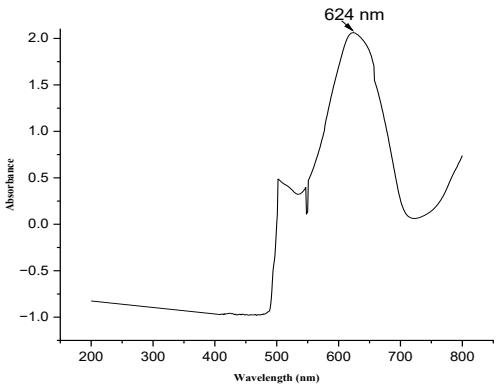


Figure 10. λ_{max} scanning of Direct Green 6 dye.

6.3. *Selection of optimum Mo content in* $Mo_xMn_{1-x}Fe_2O_4$/g-C_3N_4 *photocatalysts*

The influence of Mo inclusion on photocatalytic degradation efficacy of $Mo_xMn_{1-x}Fe_2O_4$/g-C_3N_4

nanocomposites were evaluated by varying the Mo concentration (X= 0.1-0.5) and assessing the samples performance in degrading Direct Green 6 (DG)-6 dye in **Figure 11**. The pure g-C_3N_4 had a degradation efficiency of 55.1%, whereas the Mo-modified ferrite/g-C_3N_4 nanocomposites showed enhanced photocatalytic performance. The degradation rate was slowly increased from 55.7% (x= 0.1) to 69.5% (x = 0.5) and proving that the incorporation of Mo has a positive impact on the photocatalytic behavior of the ferrite/g-C_3N_4 heterostructure.

The increase in the photocatalytic efficiency with incorporation of ferrite can be imputed to the synergetic connection between $Mo_xMn_{1-x}Fe_2O_4$ and g-C_3N_4. The mixed spinel ferrite is beneficial by improving visual-light absorption and providing more active sites, but the combination with g-C_3N_4 is advantageous to interfacial charge transfer and prevents electron-hole recombination. It has been observed that ferrite-based g-C_3N_4 heterojunctions also undergo a similar enhancement, with the addition of magnetic ferrite nanoparticles enhancing charge separation efficiency and the production of reactive oxygen species that degrade organic dyes (Iqbal *et al.* 2021; Mazaheri *et al.* 2025).

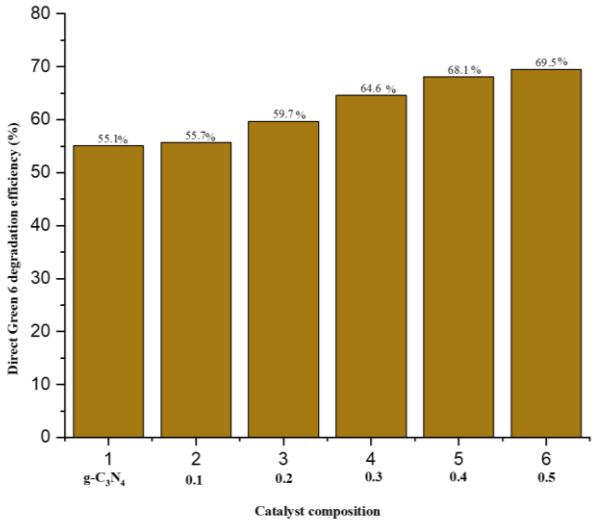


Figure 11. Photocatalytic degradation efficiency of Direct Green 6 dye over pristine g-C_3N_4 and $Mo_xMn_{1-x}Fe_2O_4$/g-C_3N_4 nanocomposites with different Mo contents ((x: 0.1-0.5).

The progressive increase in activity as the content of Mo increases could be due to the change in the electronic structure of the ferrite phase. Incorporation of Mo into spinel lattice may introduce defect states and enhance migration of charge carriers, which enhances the photocatalytic reaction. Similar results were found in Mo-based semiconductor photocatalysts, where optimal dopant concentration increased the use of visible light and the ability to produce photocatalytic outcomes, but further addition of dopant leads to the creation of recombination centers and the decrease in photocatalytic activity (Ahsan *et al.* 2025; Cao *et al.*, 2017). In the current study, the maximum activity was achieved at x = 0.5, which means that this concentration of Mo offers a balance between charge separation and light absorption and the available active sites.

The obtained trend is also consistent with previous studies on ferrite/g-C_3N_4 composites. To illustrate, g-C_3N_4 based on $NiMnFe_2O_4$ and Fe_3O_4 heterostructures have shown better degradation characteristics than their constituent parts owing to the increased interfacial contact and effective transfer of charge (Iqbal *et al.* 2021). Thus, out of all the prepared compositions, $Mo_{0.5}Mn_{0.5}Fe_2O_4$/g-C_3N_4 was chosen as the best photocatalyst to conduct the research on the characterization and optimization of CCD. The further CCD optimization of the working parameters enhanced the degradation efficiency to 97.35% under optimum conditions.

6.3.1. Optimization Experiment Variables vs Central Composite Designs for the DG6 dye

Direct Green 6 dye was degraded photocatalytically with the help of $Mo_{0.5}Mn_{0.5}Fe_2O_4$/g-C_3N_4 nanocomposites by optimizing the effect of dye concentration, catalyst dosage, pH, H_2O_2 concentration, and temperature with the help of Central Composite Design (CCD). Optimal conditions in terms of dye concentration (0.01 g/L), catalyst dosage (1 mg), pH of the solution (10), concentration of H_2O_2 (0.07 M), and temperature (90 °C) yielded a maximum degradation efficiency of 97.35%.

The concentration of the dye had a great influence on the degradation efficiency. The maximum removal efficiency was attained with the lowest dye concentration (0.01%) and an increase in the dye concentration led to a reduction in the degradation efficiency. The decreased penetration of the visible light into the highly concentrated dye solutions and the enhanced competition of the dye molecules with the active sites of the photocatalyst can explain this behavior. The same behavior observed with g-C_3N_4 based photocatalytic systems, in which a decrease in the concentration of the pollutant enhances the utilization of light and the effective interaction of the dye molecules and the catalyst active sites (Bhatti *et al.* 2020; Alibeigi *et al.* 2025).

The dosage of the catalyst was also a factor that affected the photocatalytic performance. The efficiency of degradation was increased with the addition of catalyst, because more active sites were available and more reactive oxygen species were formed. However, due to overloading catalysts can form particles and light scattering, leading to a decrease in photocatalytic efficiency. The same effects have been observed in the case of ferrite/g-C_3N_4 based photocatalysts (Ahsan *et al.* 2025; Iqbal *et al.* 2021; Imran *et al*. 2025).

Solution pH was found to be an important factor controlling dye degradation. The greatest degradation efficiency (97.35%) was achieved in the alkali environment at pH 10. It is possible that the increased activity at alkaline pH is connected to an increased surface interaction of the photocatalyst and dye molecules and increased hydroxyl radical's formation, which is involved in oxidative degradation reactions. Likewise, ferrite- g-C_3N_4 based heterojunction photocatalysts have been shown to exhibit

similar pH-dependent photocatalytic behavior (Alibeige *et al.* 2024; Weldekirstos *et al*., 2024).

Another factor that had a strong impact on degradation efficiency was H_2O_2 concentration. The best concentration of H_2O was determined as 0.07 M, which gives maximum dye removal. At this concentration, H_2O_2 will be an electron acceptor and will enhance the existence of hydroxyl radicals. Nevertheless, when H_2O_2 is in excess amounts, it can cause radical scavenging reactions, lowering the concentration of active radicals to degrade dyes (Zhang *et al.* 2024).

Temperature change also had an effect on the photocatalytic reaction. Optimization of CCD conditions produced the maximum degradation efficiency at 90 °C. The increased reaction rate at high temperature could be because of better reaction kinetics and higher contact of dye molecules with active sites on catalysts. Nevertheless, high temperature rise can have adverse effects on photocatalytic reactions through the facilitation of charge carrier recombination and depletion of radicals. CCD optimization showed that the $Mo_{0.5}Mn_{0.5}Fe_2O_4$/g-C_3N_4 nanocomposite had an excellent photocatalytic degradation performance under optimal reaction conditions, which supports the significance of optimization of the operational parameters to attain an efficient Direct Green 6 dye removal (Ahsan *et al.* 2025; Kaur *et al.* 2025; Sarkar and Bhattacharjee, 2026).

6.3.2. Statistical study

Table 2. Statistical response surface table of Direct Green 6 dye.

Dye concentration (%)	Catalyst dose	pH	H_2O_2	Temperature	Dye degradation (%)
0.01	1	4	0.01	90	27.73
0.07	1	4	0.01	30	13.74
0.01	7	4	0.01	30	29.14
0.07	7	4	0.01	90	14.56
0.01	1	10	0.01	30	90.34
0.07	1	10	0.01	90	21.13
0.01	7	10	0.01	90	95.69
0.07	7	10	0.01	30	28.44
0.01	1	4	0.07	30	26.34
0.07	1	4	0.07	90	20.45
0.01	7	4	0.07	90	28.45
0.07	7	4	0.07	30	23.67
0.01	1	10	0.07	90	97.35
0.07	1	10	0.07	30	22.91
0.01	7	10	0.07	30	96.12
0.07	7	10	0.07	90	20.45
0.02	4	7	0.04	60	56.17
0.07	4	7	0.04	60	19.67
0.04	1	7	0.04	60	38.51
0.04	7	7	0.04	60	39.13
0.04	4	1	0.04	60	0
0.04	4	10	0.04	60	79.56
0.04	4	7	0.01	60	37.76
0.04	4	7	0.07	60	37.44
0.04	4	7	0.04	30	38.91
0.04	4	7	0.04	90	42.13
0.04	4	7	0.04	60	41.44
0.04	4	7	0.04	60	41.39
0.04	4	7	0.04	60	40.99
0.04	4	7	0.04	60	40.18
0.04	4	7	0.04	60	41.13
0.04	4	7	0.04	60	40.55

Analysis of variance (ANOVA) showed that the developed quadratic model was very significant (F= 22289.83, $p < 0.001$), which means that the factors chosen correctly explained the response. The model had a great fit with a R^2 value of 99.94%. This meant that the model could explain almost all the variation in the response. The linear terms that made a difference were dye concentration ((F = 1494.81, $p < 0.001$), followed by pH ($p < 0.001$), temperature ($p = 0.001$), and catalyst dose ($p = 0.033$), H_2O_2, on the other hand, did not make a difference ($p=0.115$). Significant quadratic effects were observed for catalyst dose ($p = 0.002$), pH ($p = 0.012$), and H_2O_2 ($p < 0.001$), indicating curvature in the response surface and the possibility of optimum operating levels. Several interaction terms significantly affected the response, particularly dye concentration × pH (F = 2535.96, $p < 0.001$), which was the

strongest interaction effect among all, followed by catalyst dose × H_2O_2, dye concentration × catalyst dose, pH × temperature, and H_2O_2 × temperature. This shows that the response surface is curved and that there may be best working levels. The lack-of-fit test did not show any significant differences (p =0.206), which meant that the model accurately reflected the experimental data and could be used accurately predict and improve the process conditions. The surface plots below show these relationship effects in **Figure 12**.

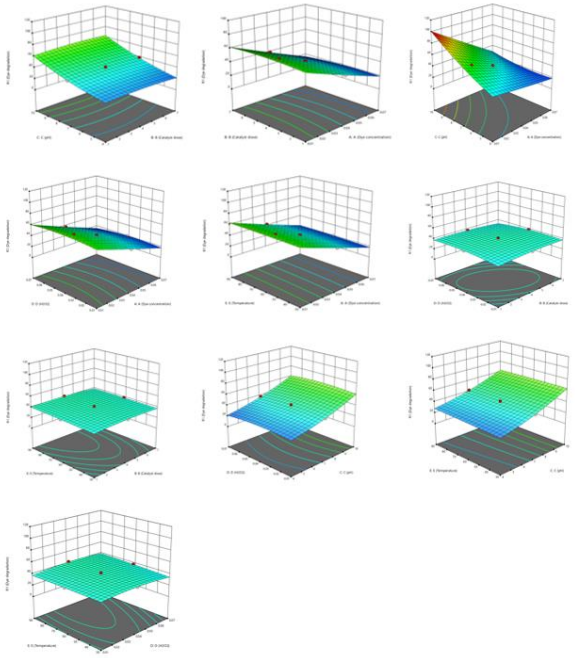


Figure 12. Anova Model.

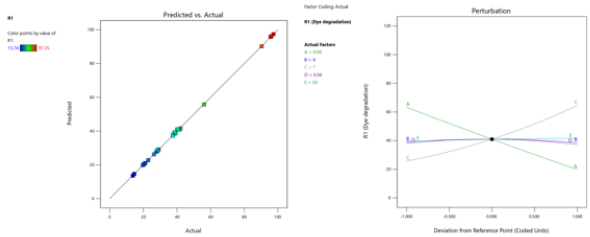


Figure 13. The above predicted vs actual plot shows the adequacy of the fitted model which is very high.

The perturbation plot indicates that the response (dye degradation) is most sensitive to factor A (dye concentration), which shows a strong negative effect as its level increases. Factor C also has a notable positive effect, improving dye degradation with increasing levels. In contrast, factors B, D, and E have nearly flat trends, indicating minimal influence on the response within the studied range. Overall, the process is primarily governed by factors A and C, while the remaining variables play a negligible role.

6.4. *Kinetics and Adsorption Isotherm Studies*

The adsorption behavior of Direct Green 6 dye onto $Mo_{0.5}Mn_{0.5}Fe_2O_4$/g-C_3N_4 nanocomposite was investigated and the Langmuir and Freundlich isotherm models were used. The Langmuir plot (Ce/qe vs Ce) was linear and had a high correlation coefficient (R^2 = 0.9121), which corresponds to the adsorption process being close to an on a homogeneous surface. This indicates that all the active sites are equally active for the dye molecules and that any time a site is filled, no more dye molecules are adsorbed on that site, which is common for ferrite/g-C_3N_4 composites reported in literature. The Freundlich plot of log (qe) vs log(Ce) had a lower correlation coefficient (R^2 = 0.2766), which means that the Freundlich model was not well appropriate for the adsorption of the iron ore sample. This means that surface heterogeneity has less of an effect on this system and that is less significant. The strong Langmuir consistency has been observed with the weak Freundlich fit, suggesting that the adsorption is mainly in the form of a monolayer and that all active sites have similar energies. The maximum monolayer adsorption capacity was also estimated using the Langmuir model, which shows the efficacy of the nanocomposite in the removal of dye under the optimum conditions. A good R^2 value indicates that the nanocomposite has enough adsorption sites with sufficient energy similarity, which facilitates the decolorization of the Direct Green 6 molecules (Iqbal *et al.* 2021; Michalska *et al.* 2024).

Different studies have shown that ferrite-based magnetic nanocomposites are very good at absorbing dyes because the metal oxide nanoparticles and carbon nitride frameworks work together to make them stronger. Tabbasum *et al.* (2024) talked about Ag-CO ferrite-based magnetic materials that were used to get rid of dyes. They followed both Langmuir and Freundlich models with R^2 values 0.99 and 0.97. The highest amount of dye that could be absorbed was estimated to be 45.66 mg g^{-2}, and the rate of absorption followed by the pseudo-second order model. This shows that the presence of active sites and surface interactions has a big effect on how dye is absorbed. Wu *et al.* (2024) studied lanthanum-modified mesoporous g-C_3N_4 composites and found that the Langmuir model better explained the adsorption of organic pollutants, pointing to a mostly monolayer adsorption process with uniform active sites. These results confirm that $Mo_{0.5}Mn_{0.5}Fe_2O_4$/g-C_3N_4 exhibits Langmuir adsorption characteristics with significant correlation values (R^2= 0.9121).

The isotherm and adsorption capacity characteristics of the current composite are similarly aligned with previously documented magnetic g-C_3N_4 composite had a peak adsorption ability of 24.9 mg g^{-1} with Langmuir and Freundlich fitting coefficients of R^2= 0.9836 and 0.9872, attributed to the adsorption sites derived from Fe_2O_4 nanoparticles and g-C_3N_4 sheets (Xu and Peng, 2019; Moied *et al*., 2026). In contrast, the current $Mo_{0.5}Mn_{0.5}Fe_2O_4$/g-C_3N_4 composite exhibited a similar adsorption capacity (qmax= 21.93 mg g^{-1}) with a predominant Langmuir model, suggesting a better-regulated adsorption interface for Direct Green 6 molecules. The disparity in adsorption capacity and model fitting across several investigations may be attributed to differences in ferrite composition, surface area, pore structure, pollutant molecular dimensions and interactions between metal oxide nanoparticles and carbon nitride layers. Consequently, the finding obtained validate that the synthesised mixed ferrite/g-C_3N_4 nanocomposites exhibit favorable

adsorption properties for effective dye elimination and subsequent photocatalytic degradation

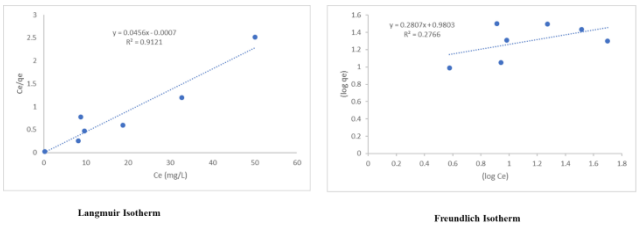


Figure 14. Kinetics and Mechanism graph.

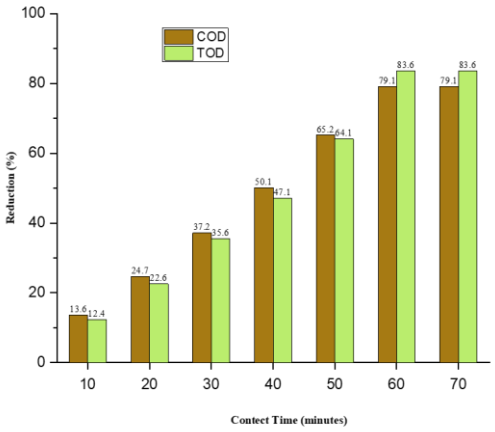


Figure 15. Reduction (%) of COD and TOC with various time levels.

6.5. *Mineralization study*

Treated solutions were analyzed for TOC and COD. Significant reductions in TOC and COD were observed, confirming effective mineralization of dye molecules. The mineralization efficiency of $Mo_{0.5}Mn_{0.5}Fe_2O_4/g\text{-}C_3N_4$ is higher than previous composites based on $g\text{-}C_3N_4$, which showed a TOC removal of 70–80%. The COD and TOC tests were done to assess the performance of the nanocomposite of $Mn_{0.5}Mn_{0.5}Fe_2O_4/g\text{-}C_3N_4$ for mineralization of the Direct Green 6 (DG6) dye during degradation. The extent of organic pollutant oxidation and mineralization (decolorization) in heterogeneous photocatalytic systems is commonly quantified by COD and TOC values. Researchers have found that $g\text{-}C_3N_4$ based composite photocatalysts are very good for removal of organic matter. For example, nanocomposites of $g\text{-}C_3N_4$ and magnetic ferrites have been shown to have COD and TOC reduction in pollutants solutions, which proves that organics are mineralized in a big way. Under the optimum conditions, the COD and TOC of the treated Direct Green 6 (DG6) dye solution reduced significantly with a catalyst of $Mn_{0.5}Mn_{0.5}Fe_2O_4/g\text{-}C_3N_4$. The measured percent reduction in COD (79.1%) and TOC (83.6%) indicate that the nanocomposite not only decolorized the dye, but also degraded the organic molecules towards complete oxidation to CO_2/H_2O, thus improving water quality. High percent removal of COD and TOC demonstrates the excellent catalytic potential of the $Mn_{0.5}Mn_{0.5}Fe_2O_4/g\text{-}C_3N_4$ nanocomposite for wastewater purification, similar to other reported advanced photocatalytic systems where TOC removals of >90 % and substantial COD reduction were achieved, indicating efficient mineralization. The results are supported by different literature (Gaur *et al.* 2026; Mosleh *et al.* 2021; Dippong *et al*. 2021).

6.6. *Catalyst Reusability*

Reusability of the $Mo_{0.5}Mn_{0.5}Fe_2O_4/g\text{-}C_3N_4$ nanocomposite was evaluated by performing multiple cycles of Direct Green 6 (DG6) degradation under visible light. The photocatalytic activity of the catalyst remained high for five cycles (as presented in **Figure 16**). In the first cycle, 83.4% of the dye was decolorized, and in the fifth cycle, 73.4%, showing that there was no significant loss of catalytic performance. Such a slight drop in performance can be attributed to possible surface fouling. However, the comprehensive findings highlight the good durability and reusability of the nanocomposite for wastewater treatment applications. The excellent stability is attributed to the robust heterojunction and magnetic ferrite core, enabling easy recovery and minimal structural loss. Other $g\text{-}C_3N_4$-based composites also demonstrate good reusability (3–5 cycles) with only a small decrease in activity (Rajendran *et al.* 2021; Ahsan *et al.* 2025; Kiran *et al*., 2026).

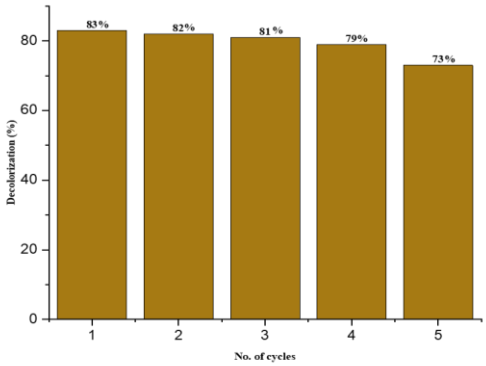


Figure 16. Catalyst reusability.

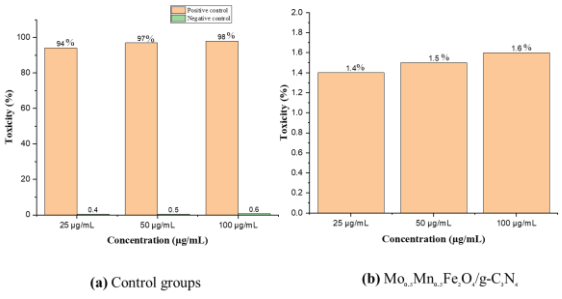


Figure 17. Toxicity effect of $Mo_{0.5}Mn_{0.5}Fe_2O_4/g\text{-}C_3N_4$ nanocomposite and control groups at different concentrations: (a) control groups and (b) nanocomposite toxicity response.

6.7. *Toxicity Analysis*

The hemolytic activity and general biocompatibility of the chemically synthesized nanocomposite were systematically investigated to determine possible interactions with erythrocyte membranes and cytotoxic effects, a factor that is crucial for environmental and biomedical applications like photocatalytic degradation of Direct Green 6 dye (DG6). Hemolysis of the nanocomposite was very poor, with hemolysis concentrations of 25, 50, and 100 ug/mL as indicated in **Figure 17**. The positive control, however, showed the same levels at the same concentrations, and the negative control stayed below,

which indicated stability of the baseline levels. The findings suggest that the $Mo_{0.5}Mn_{0.5}Fe_2O_4/g\text{-}C_3N_4$ composite has minimal effects on the integrity of the red blood cells, consistent with other studies involving ferrite/g-C_3N_4 composites that have shown that the carbon nitride material helps to stabilize metal oxide nanoparticles, minimizing both oxidative stress and membrane damage (Muhammad *et al.* 2025). Minimal hemolytic activity observed confirms the biocompatibility of the composite and its ability to be used in environmental applications where the selective photocatalytic degradation of dyes does not affect non-target organisms significantly.

6.8. *Proposed degradation pathway of Direct Green 6 dye*

$Mo_{0.5}$ $Mn_{0.5}Fe_2O_4/g\text{-}C_3N_4$ nanocomposite irradiation is shown in **Figure 18**. The first step involves the Direct Green 6 dye molecules attaching to the surface of the nanocomposite by interacting with the available active sites. When visible light is irradiated, the $Mo_{0.5}Mn_{0.5}Fe_2O_4/g\text{-}C_3N_4$ heterostructure absorbs photon energy and produces photogenerated electron-hole (e^-/h^+) pairs. The formation of a close heterojunction interface between Mo-modified manganese ferrite and g-C_3N_4 enables interfacial charge transfer and decreases the chance that photogenerated electrons (e^-) and holes (h^+) will combine again. In the first step of degradation of our target dye, only the sulphonate group, which is close to the azo chromophoric group, was desulphonated, followed by the desulphonation of the other sulphonate group, which was on a more sterically hindered site of the azo group. Photocatalytic degradation via hydroxyl radical/hole attack is not a single concerted step, it proceeds through sequential, site-selective oxidative attack (Chowdhury et al. 2024). It has been corrected now. The electron-deficient nitro-substituted fragment generated at this stage becomes accessible for reduction by photogenerated conduction-band electrons (e^-). Nitro-group reduction via photogenerated electrons is a well-documented reductive pathway in AOP-based dye/nitroaromatic degradation (Mazzanti *et al*. 2020). Conduction band electron-hole coupling with dissolved oxygen molecules (O_2) results in superoxide radicals ($\cdot O^{2-}$). In the meantime, during photogeneration, holes are created in the valence band, oxidizing the surface hydroxyl groups (OH) or water molecules (H_2O) to hydroxyl radicals ($\cdot OH$). These oxidative species are the most commonly used agents that lead to the breakdown of DG6. The generated $\cdot O_2^-$ and $\cdot OH$ radicals damage the chromophoric groups and aromatic structures of Direct Green 6 molecules, leading to azo (-N=N-) bonds, C-N bonds, and other organic functional groups. As a result, the dye molecules are broken down into small intermediate compounds, which further undergo oxidation reactions in the presence of continuous visible-light irradiation. Lastly, these intermediates are mineralized to relatively harmless compounds like O_2, H_2O, and inorganic ions.

The synergistic effects of the addition of Mo and the formation of heterojunctions can explain the improvements in the photocatalytic performance of $Mo_{0.5}Mn_{0.5}Fe_2O_4/g\text{-}C_3N_4$. The mixing of molybdenum changes the electronic structure, offers more active sites, enhances the use of visible light, and facilitates the movement of charges. Therefore, the $Mo_{0.5}Mn_{0.5}Fe_2O_4/g\text{-}C_3N_4$ heterostructure is an efficient route to enhance charge separation and expedite the process of degradation.

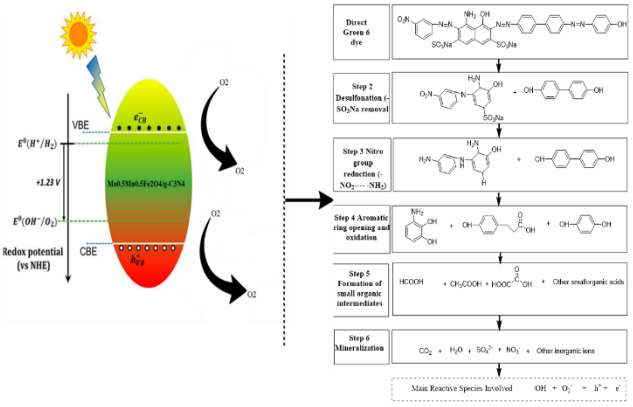


Figure 18. Proposed mechanism of degradation of Direct Green 6 dye (DG6) over $Mo_{0.5}$ $Mn_{0.5}$ $Fe_2O_4/g\text{-}C_3N_4$ nanocomposite under visible-light irradiation.

6.9. *Environmental impact*

$Mo_{0.5}Mn_{0.5}Fe_2O_3/g\text{-}C_3N_4$ NCs can be used as a photocatalytic substance for industrial wastewater treatment, particularly textile wastewaters, because of its environmental friendliness. The addition of Mo, Mn, and Fe-based oxides with graphitic carbon nitride further improves the visible-light absorption, charge separation, and creation of ROS (oxygen free radicals), which decompose complex dye molecules to form simple and less toxic ones. The benefit of the presence of g-C_3N_4 is that no metal, is chemically stable, relatively low cost, and environmentally friendly, and the mixed metal oxide phase enhances the catalytic efficiency and reusability. This combination helps lower the dye content, color strength, organic matter, and potential toxicity of the wastewater, resulting in cleaner water bodies. Note that potential environmental issues should also be taken into account, however. As the catalyst is used repeatedly, metal ions like Mo, Mn, or Fe can leach off the surface of the catalyst and can accumulate in water or soil, causing toxicity to aquatic organisms at higher concentrations. If the mineralization is incomplete, the degradation of azo or reactive dyes also generates intermediate aromatic compounds, which sometimes are also more toxic than the original dye. Therefore, before scale-up, it would be important to consider proper recovery and reuse of the catalyst, stability testing, and assessment of leaching. In summary, $Mo_{0.5}Mn_{0.5}Fe_2O_3/g\text{-}C_3N_4$ is a promising material for eco-friendly and efficient photocatalytic degradation of dye-contaminated effluents under controlled conditions in combination with appropriate after-treatment recovery (Lopez Medina *et al.* 2025; Wu *et al.* 2024).

7. Conclusions

$Mo_{0.5}Mn_{0.5}Fe_2O_4/g\text{-}C_3N_4$ nanocomposites were efficiently synthesized and investigated as photocatalysts activated by visible-light for the degradation of Direct Green 6 dye (DG6). Among the estimated composites of various Mo

contents (x = 0.1-0.5), $Mo_{0.5}Mn_{0.5}Fe_2O_4$/g-C_3N_4 had the best photocatalytic capability due to the enhanced absorption of visible-light, the interfacial interaction, and the separation of the generated charge carriers. The presence of the heterostructure was confirmed using several characterization methods, such as UV-vis spectroscopy, XRD, SEM, EDX, FTIR, and zeta potential, which confirmed the integration of $Mo_{0.5}Mn_{0.5}Fe_2O_4$ nanoparticles with the g-C_3N_4 matrix. CCD was used to optimize the photocatalytic degradation process, where the process variables were assessed as important, including dye concentration, catalyst dosage, pH, H_2O_2 concentration, and temperature. The optimum values were achieved under the following conditions: dye concentration of 0.01%, catalyst dosage (1mg), pH (10), concentration of H_2O_2 of 0.07 M and temperature of 90 °C, which produced the highest degradation efficiency of DG6 of 97.35%. The statistical analysis showed that the quadratic model developed was quite significant and could be used to predict the photocatalytic response. The kinetic study showed that the degradation of DG6 was a pseudo-first-order reaction. Adsorption analysis revealed that the Langmuir model provided a better fit than the Freundlich model when it came to adsorption analysis. This meant that monolayer adsorption on a relatively uniform active sites was a part of the degradation process. The efficiency of nanocomposite in mineralization was also validated through mineralization studies in which there was a considerable reduction in COD (79.1%) and TOC (83.6%), implying that organic dye molecules were greatly oxidized and smaller oxidation products were formed. The $Mo_{0.5}Mn_{0.5}Fe_2O_4$/g-C_3N_4 exhibited excellent photocatalytic activity during five consecutive degradation cycles, maintaining high activity with only a slight decrease in efficiency. Moreover, toxicity analysis revealed that there was low hemolytic activity, which indicated that the synthesized composite was less likely to cause environmental hazards. In sum, the $Mo_{0.5}Mn_{0.5}Fe_2O_4$/g-C_3N_4 nanocomposite has a great perspective in terms of a stable, efficient and reusable photocatalyst to treat dye-contaminated wastewater. Further studies may concentrate on enhancing the photocatalytic method, assessing actual industrial effluents, and investigating the durability of catalysts during prolonged use.

8. Prospects of Research in the Future

The use of this nanocomposite in wastewater treatment may facilitate the creation of an environmentally favorable and sustainable method. The straightforward chemical technique was used for the fabrication of the nanocomposite. The synthesized nanocomposite was used in the photocatalytic breakdown of the specified dye and holds promise for the treatment of wastewater (textile wastewater). The nanocomposite is a stable and efficient photocatalyst when exposed to light and can be applied in the treatment of dye contaminants in wastewater. In addition to its use in industrial effluent treatment, this nanocomposite may be used for purifying polluted water in rivers, lakes, and aquifers. The photocatalytic property might be considered a beneficial characteristic regarding the potential for remediating anthropogenically stressed natural water systems, since it transforms more complex organic contaminants into simpler, less dangerous molecules.

Acknowledgement

The authors want to thank the Department of Applied Chemistry, Government College University, Faisalabad, Pakistan, and National Textile University, Faisalabad, Pakistan for providing the necessary research facilities required for this study. This research is the part of doctoral dissertation of Ms. Azqa Amjad.

Author contributions

AA: doing experimental, writing original draft; SK & MBQ: conceptualization, supervision, draft checking; MNA: technical evaluation, data interpretation; SA: review and editing. All authors read and approved the final manuscript.

Availability of data and materials

All data analyzed during this research work are presented in this article.

Ethics approval consent to participate

Not applicable.

Consent for publication

Not applicable.

Competing interests

The authors declare no competing interests.

References

Ahsan O., Ehsan H., Tahir F., Nadeem S., Murtaza M., Kmal M. S. and Althobiti R. A. (2025). Fabricating and applications of vanadium doped molybdenum ferrites NPs/Sg-C3N4 composites for photocatalytic degradation of dyes. Polyhedron, 279, 117-662. https://doi.org/10.1016/j.poly.2025.117662

Akechatree N., Lakshmanan K., Rajendran R., Rojviroon T., Rojviroon O. and Sirivithayapakorn S. (2025). Bifunctional MnFe2O4/g-C3N4 nanocomposites for synergistic electrocatalytic oxygen evolution and photocatalytic organic dye degradation. Journal of Water Process Engineering, 77, 108-590. https://doi.org/10.1016/j.jwpe.2025.108590

Akhtar N., Nadeem N., Yaseen M., Jilani A., Mahmood A., Zubair U. and Zahid M. (2024). Solar light-driven photocatalytic degradation potential of g-C3N4 based binary chalcogenides (AgBiS2/g-C3N4). Materials Chemistry and Physics, 316, 12-9067. https://doi.org/10.1016/j.matchemphys.2024.129067.

Alibeigi A. N., Pormazar S. M., Salmani M. H. and Dalvand A. (2025). Heterogeneous Fenton process using GO@ Fe3O4/Cu catalyst for the degradation of reactive dyes from aqueous solutions: modeling and optimisation. International Journal of Environmental Analytical Chemistry, 105(16), 4459-4476. https://doi.org/10.1080/03067319.2024.2371033.

Arunprasad V., Thulasi S., Abdulrasool M. M. and Hema K. M. (2026). Synergistic Design of Cu-Zn Ferrite–g-C3N4 Hybrid Nanocomposite for Solar-Driven Pollutant Degradation and Dye-Sensitized Solar-Cell Applications: Arunprasad, Thulasi,

Abdulrasool, and Hema Kumar. Journal of Electronic Materials, 55(1), 547-564. https://doi.org/10.1007/s11664-025-12528-9.

Bakht M. A., Alharthi A. I., Alotaibi M., and Ali M. I. (2025). A visible-light-sensitive molybdenum ferrite oxide/titanium dioxide nanocomposite photocatalyst: MA Bakht et al. Research on Chemical Intermediates, 51(9), 5183-5210. https://doi.org/10.1007/s11164-025-05683-5.

Bharathi S. D. and Babu D. R. (2024). Synthesis, characterization and antimicrobial activity of Manganese ferrite nanoparticles. Materials Science and Engineering: B, 300, 11-7051. https://doi.org/10.1016/j.mseb.2023.117051.

Bhatti H. N., Iram Z., Iqbal M., Nisar J., and Khan, M. I. (2020). Facile synthesis of zero valent iron and photocatalytic application for the degradation of dyes. Materials Research Express, 7(1), 015-802. https://doi.org/10.1088/2053-1591/ab66a0.

Cao Y., Gao Q., Li Q., Jing X., Wang S. and Wang W. (2017). Synthesis of 3D porous MoS2/g-C3N4 heterojunction as a high-efficiency photocatalyst for boosting H2 evolution activity. RSC Advances, 7(65), 40727-40733. https://doi.org/10.1039/c7ra06774g.

Chowdhury, A.P., Chinnam, S., Anantharaju, K.S., Kumar, B.S., Keshavamurthy, K., Gurushantha, K. (2024). Synthesis of GS-assisted Mn5O8 photocatalysts for efficient visible-light degradation of direct green 6 dye. Ionics. https://doi.org/10.1007/s11581-026-07386-2

de Oliveira, C. R. S., de Oliveira, P. V., de Aguiar, G. C. O., Missner, M. E. P., Tewo, R. K., da Silva Júnior, A. H., ... & de Aguiar, C. R. L. (2025). Dyes and dyeing of textiles: an overview of sustainability issues. Sustainable Coloration Techniques in Textiles, 1-54. https://doi.org/10.1007/978-981-96-4975-4_1.

Devi E. C. and Soibam I. (2017). Structural and optical characterization of MnFe2O4 nanoparticles. Advanced Materials Proceedings, 2(2), 93-96. https://doi.org/10.5185/amp.2017/206.

Dippong T., Levei E. A. and Cadar O. (2021). Recent advances in synthesis and applications of MFe2O4 (M= Co, Cu, Mn, Ni, Zn) nanoparticles. Nanomaterials, 11(6), 1560. https://doi.org/10.3390/nano11061560.

El-Sayyad G. S., Abd Elkodous M., El-Khawaga A. M., Elsayed M. A., El-Batal A. I. and Gobara M. (2020). Merits of photocatalytic and antimicrobial applications of gamma-irradiated Co x Ni1− x Fe2O4/SiO2/TiO2; x= 0.9 nanocomposite for pyridine removal and pathogenic bacteria/fungi disinfection: implication for wastewater treatment. RSC Advances, 10(9), 5241-5259. https://doi.org/10.1039/c9ra10505k.

Estrada-Movilla, E., Castillo-Saenz, J., Valdez-Salas, B., Ortiz-Pérez, Á., Beltrán-Partida, E., Salvador-Carlos, J., & Puello-Polo, E. (2025). Challenges and opportunities for g-C3N4-based heterostructures in the photodegradation of environmental pollutants. Catalysts, 15(7), 653.

Gaur R., Parmar H., Patel J., Mhaske P., Pathak G., Taneja N. and Shahabuddin S. (2026). Machine learning-driven performance prediction of Z-scheme g-C3N4/SnS2 heterostructure photocatalyst for complete mineralization of indigo carmine and elucidation of degradation pathways. Scientific Reports, 16(1), 1-17. https://doe.org/s41598-026-37528-5.

Gupta N. K., Ghaffari Y., Kim S., Bae J., Kim K. S. and Saifuddin M. (2020). Photocatalytic degradation of organic pollutants over MFe2O4 (M= Co, Ni, Cu, Zn) nanoparticles at neutral pH. Scientific Reports, 10(1), 49-42. https://doi.org/s41598-020-61930-2

Hassanzadeh S., Farhadi S. and Moradifard F. (2023). Synthesis of magnetic graphene-like carbon nitride-cobalt ferrite (g-C3N4/CoFe2O4) nanocomposite for sonocatalytic remediation of toxic organic dyes. RSC advances, 13(16), 10940-10955. https://doi.org/10.1039/d3ra00057e.

Horta A. C., Poças A., Amaral J. S. and Amorim C. O. (2025). Fine-Tuning of Mn-Ferrite nanoparticle size using a Dual-Base coprecipitation method. Materials Science and Engineering: B, 314, 11-8058. https;//doi.org/10.1016/j.mseb.2025.118058.

Imran, M., Abdullah, A. Z., Rashid, M. S., Bakather, O. Y., Alshoaibi, A. M., Khan, M. E., ... & Chaudhary, A. A. (2025). Controlled morphology of g-C3N4/metal oxide-based nanostructures applications in organic pollutant photodegradation: A review. Inorganic Chemistry Communications, 115681.

Iqbal N., Afzal A., Khan I., Khan M. S. and Qurashi A. (2021). Molybdenum impregnated g-C3N4 nanotubes as potentially active photocatalyst for renewable energy applications. Scientific Reports, 11(1), 16-886. https://doi.org/s41598-021-96490-6.

Ismael M. and Wark M. (2022). Photocatalytic activity of CoFe2O4/g-C3N4 nanocomposite toward degradation of different organic pollutants and their inactivity toward hydrogen production: The role of the conduction band position. FlatChem, 32, 100-337. https://doi.org/10.1016/j.flatc.2022.100337.

Joseph R., Ashkar M. A., Babu A., Rani S. K., Gallo J., Mamat M. H. and Vasimalai N. (2026). Recent advances in the synthesis of g-C3N4 nanocomposites for energy conversion and environmental remediation applications. Sustainable Energy & Fuels, 3(1), 1-15. https://doi.org/10.1039/d5se01533b.

Kaur J., Tewari S., Kaur A., and Malik, R. (2025). Dye and dye-containing hazardous waste in water resource. In Emerging Contaminants in Water and Wastewater: Sources and Substances, 179-199. Cham: Springer Nature Switzerland. https://doi.org/10.1007/978-3-031-82579-8_8.

Khaliq N., Bibi I., Majid F., Kamal S., Alwadai N. A., Taj B. and Iqbal M. (2026). Dual-ion engineered spinel ferrites: structural, optical and ferroelectric responses of Mn/Co doped $MgFe_2O_4$ prepared via hydrothermal approach. Polyhedron, 289(1), 118010. https://doi.org/10.1016/j.poly.2026.118010.

Kiran S., Ahmed F., Naheed S., Batool U., Batool A., Abbas M. A. and Gulzar T. (2025). Degradation of Indigo Blue dye in wastewater by green synthesized Ni-Zn oxide nanohybrid: an environmental remediation approach. Desalination and Water Treatment, 101-430. https://doi.org/10.1016/j.dwt.2025.101430.

Kiran S., Albargi H. B., Afzal G., Aimun U., Anjum M. N., Qadir M. B. and Abdullah, M. M. (2023). Azadirachta indica-assisted green synthesis of magnesium oxide nanoparticles for degradation of Reactive Red 195 dye: a sustainable environmental remedial approach. Applied Water Science, 13(10), 1-93. https://doi.org/10.1007/s13201-023-02000-6.

Kiran, S., Jamal, A., Hassan, S. U. U., Hussain, M., Hussain, M., Abbas, M., & Yousaf, A. (2026). Carthamus tinctorius-mediated synthesis of zinc oxide nanoparticles and evaluation of biological and Dye Degradation Activities. Journal of Environmental Science and Management, 29(1), 16-28.

Lopez Medina J. A., Domínguez D., Pizá P., Liu G., Velez C., Reyes Gómez F. and Mejía-Salazar J. R. (2025). Magnetic photocatalyst nanocomposite based on MnFe2O4@ ZnO for AZO dye degradation. ACS Omega, 10(17), 17595-17610. https://doi.org/10.1021/acsomega.4c11468.

Lu M., Javed M., Javed K., Tan S., Iqbal S., Liu G. and Farouk A. E. (2022). Construction of a well-defined S-scheme heterojunction based on Bi-ZnFe2O4/Sg-C3N4 nanocomposite photocatalyst to support photocatalytic pollutant degradation driven by sunlight. Catalysts, 12(10), 11-75. https://doi.org/10.3390/catal12101175.

Ma H. and Liu C. (2021). A mini-review of ferrites-based photocatalyst on application of hydrogen production. Frontiers in Energy, 15(3), 621-630. https://doi.org.10.1007/s11708-021-0761-0.

Manohar, A., Suvarna, T., Vattikuti, S.V.P., Manivasagan, P., Jang, E.-S., Al-Asbahi, B.A., Kim, K.H. (2026). Comprehensive study of g-C3N4/$Zn_xMn_{1-x}Fe2O4$ nanocomposites: From structural features to electrochemical and biological performance. Ceramics International, 52(14), 24772–24786. https://doi.org/10.1016/j.ceramint.2026.04.042

Mazaheri S., Monsef R., Alsultany F. H. and Salavati-Niasari M. (2025). Enhanced visible-light-driven photocatalytic potential of magnetic NiMnFeO4/g-C3N4 nanocomposites for degradation of aqueous organic pollutants: Schiff-base ligand-assisted sol–gel auto-combustion synthesis, characterization and mechanism analysis. Applied Water Science, 15(6), 1-30. https://doi.org/10.1007/s13201-025-02469-3.

Mazzanti, M., Caramori, S., Fogagnolo, M., Cristino, V., & Molinari, A. (2020). Turning waste into useful products by photocatalysis with nanocrystalline TiO2 thin films: Reductive cleavage of azo bond in the presence of aqueous formate. Nanomaterials, 10(11), 2147.

Michalska M., Pavlovsky J., Scholtzova E., Skorna P., Matejka V., Bochenek K. and Nishihara H. (2024). A facile approach for fabricating g-C3N4-based materials as metal-free photocatalysts. Results in Engineering, 24, 103-109. https://doi.org/10.1016/j.rineng.2024.103109.

Moied, A., Kiran, S., Bentalib, A., Gulzar, T., Khaliq, Z., Qadir, M.B., Khan, N.M., Nabeel, M.I., Jumah, A.B., Shahzad, A. (2026). Green synthesis of ZnO and NiO nanoparticles for degradation of Basic Brilliant Flavine Y-40 Dye: A Sustainable Environmental Cleaner Approach. Desalination and Water Treatment, 328, 101942. https://doi.org/10.1016/j.dwt.2026.101942

Mosleh A. T., Al-Harbi F. F., Gouadria S. M., Zyoud S. H., Zahran H. Y., Hussien M. S. and Yahia I. S. (2024). Photodegradation of wastewater containing organic dyes using modified g-C3N4-doped ZrO2 nanostructures: towards safe water for human beings. Catalysts, 14(1), 1-42. https://doi.org/10.3390/catal14010042.

Muhammad E., Deepa S., Thakur P. and Thakur A. (2025). Toxicity evaluation of nanoferrites. In Nanoferrites for Emerging Environmental Applications, 489-510. Elsevier Science Ltd. https://doi.org/10.1016/B978-0-443-22232-0.00021-6.

Mukherjee, S., & Bairwa, D. H. (2025). Environmental issues arising from urbanization: A study on the ecological consequences of rapid urban growth. Journal of Humanities and Education Development, 7(3), 12-17. https://doi.org/10.22161/jhed.7.3.3.

Naz S., Kiran S., Kamal S., Sethi A., Amjad A. and Munir B. (2026). Synthesis and characterization of Biopolymer encapsulated Mmanganese oxide nanocomposite for the removal of dyes from wastewater: A step towards sustainability. Journal of Molecular Structure, 1353(1), 144651. http://doi.org/10.1016/j.molstruc.2025.144651.

Nguyen L. T. T., Duong A. T. T., Bui N. D., Ngo V. T. M., Nguyen H. Q., Nguyen H. T. T. and Tran T. V. (2025). Synthesis of magnetic NiFe2O4/g-C3N4 heterojunction photocatalysts for boosting dye degradation performance under visible-light irradiation. Nanoscale Advances, 7(2), 536-548. https://doi.org/10.1039/d4na00694a.

Pattanayak, D. S., Surana, M., Kumar, A., Singh, D., & Pal, D. (2024). Graphitic carbon nitride (g-C3N4)-based photocatalysts for dye removal: current status. Sustainable Chemistry for the Environment, 7, 100141.

Praus P., Řeháčková L., Čížek J., Smýkalová A., Koštejn M., Pavlovský J. and Kočí K. (2022). Synthesis of vacant graphitic carbon nitride in argon atmosphere and its utilization for photocatalytic hydrogen generation. Scientific Reports, 12(1), 13-622. https://doi.org/s41598-022-17940-3.

Rajendran R. (2021). Investigation on cu2o combined c3n4/zno heterostructures for high-performance photocatalytic dye degradation under visible-light exposure. Research Square, 8(1), 1-13. https://doi.org/10.21203/rs.3.rs-206595/v1.

Rasool B. S., Abbas A. K. and Haddad, R. (2025). Photocatalytic innovations in environmental remediation: mechanisms, materials, and challenges for persistent organic pollutant removal. Environmental Monitoring and Assessment, 197(10), 10-86. https://doi.org/10.1007/s10661-025-14531-3.

Salem F., Abdullah W. and Azman N. Z. N. (2026). Sustainable synthesis and multifunctional applications of manganese ferrite nanoparticles in environmental remediation and next-generation of biomedical theranostics. Journal of Environmental Chemical Engineering, 14(1), 120-989. https://doi.org/10.1016/j.jece.2025.120989.

Sarkar T. Bhattacharjee A. (2026). Green synthesized ZnO nanocatalysts for rapid and effective visible-light degradation of industrial dyes. RSC Advances, 16(3), 2671-2684. https://doi.org/10.1039/d5ra08475j.

Saxena V. (2025). Water quality, air pollution, and climate change: investigating the environmental impacts of industrialization and urbanization. Water, Air, & Soil Pollution, 236(2), 1-73. https://doi.org/10.1007/s11270-024-07702-4.

Shahverdizadeh G. H., Seyyedi K., Mehrizad A., Majdan-Cegincara R., Jamshidi S., Ghasemi E. and Es' hagi M. (2025). Recent Insights into g-C3N4 based composites for Methylene Blue Photocatalytic Degradation. Results in Engineering, 108-595. https://doi.org/10.1016/j.rineng.2025.108595.

Sharma D., Ola S. K. and Dhayal V. (2023). Precursor-directed approach to fabricate TiO2-gCN composite: An efficient photocatalyst to harness solar spectrum. Materials Research Innovations, 27(5), 318-329. https://doi.org/10.1080/14328917.2022.2157995.

Singh V. (2025). An overview on recent trends of spinel ferrites (MFe2O4: M= Fe2, Co2, Mn2, Ni2, Zn2) synthesis and catalytic applications. International Journal of New Chemistry, 12(3), 2-83.

Sinha S., Sharma R., Singh J., Kumar S., Singh R. and Jahan N. (2025). Experimental and first-principles study of an optimized cylindrical-shaped ZnO/g-C3N4 heterojunction for enhanced adsorption and photocatalytic degradation of

methylene blue dye. ACS Omega, 10(27), 28763-28781. https://doi.org/10.1021/acsomega.4c10430.

Sun S., Li J., Song P., Cui J., Yang Q., Zheng X. and Liang S. (2020). Facile constructing of isotype C3N4 (bulk)/C3N4 (nanosheet) heterojunctions through thermal polymerization of single-source glucose-modified melamine: an efficient charge separation system for photocatalytic hydrogen production. Applied Surface Science, 500, 143-985. 10.1016/j.apsusc.2019.143985.

Tabassum N., Anjum R., Haque P., Hossain M. S., Mobarak M. B., Quddus M. S. and Mahmud M. (2024). Ag–Co ferrite-based magnetic polymeric composite film: a breakthrough in cationic dye remediation for sustainable environment. RSC Advances, 14(49), 36557-36575. https://doi.org/10.1039/d4ra06315e.

Toqeer I. (2026). Ferrite-Based photocatalysts for environmental remediation and solar-driven energy conversion. Environmental Technology Reviews, 15(1), 317-372. https://doi.org/10.1080/21622515.2026.2669120.

Wang Y., Yang W. and Ding K. (2024). Synergistic Ag/g–C_3N_4 H_2O_2 system for photocatalytic degradation of azo dyes. Molecules, 29(16), 38-71. https://doi.org/10.3390/molecules29163871.

Weldekirstos, H. D., Mengist, T., Belachew, N., & Mekonnen, M. L. (2024). Enhanced photocatalytic degradation of methylene blue dye using fascily synthesized g-C3N4/CoFe2O4 composite under sun light irradiation. Results in Chemistry, 7, 101306.

Wu Z., Li Y., Jiang P., Ma S., Dong W., Zhao H. and Wang X. M. (2024). Evaluation of the adsorption and degradation performance of lanthanum-modified mesoporous carbon nitride composite materials for tetracycline wastewater treatment. New Journal of Chemistry, 48(20), 9090-9102. https://doi.org/10.1039/d4nj00864b.

Xu R. Peng Y. (2019). Preparation of magnetic g-C3N4/Fe3O4 composite and its application in the separation of catechol from water. Materials, 12(18), 28-44. https://doi.org/10.3390/ma12182844.

Zhang M., Xing M., Dong B., Zhang H., Sun X., Li Q. and Zhu H. (2023). Thermal polymerisation synthesis of g-C3N4 for photocatalytic degradation of Rhodamine B dye under natural sunlight. Water, 15(16), 2-903. https://doi.org/10.3390/w15162903.